Available online at www.sciencedirect.com
SCIENCE DIRECT®
Journal of Solid State Chemistry 177 (2004) 1838–1846
JOURNAL OF SOLID STATE CHEMISTRY
http://elsevier.com/locate/jssc

# Modelling, refinement and analysis of the "Type III" $\delta$-$Bi_2O_3$-related superstructure in the $Bi_2O_3$–$Nb_2O_5$ system

Christopher D. Ling* and Mark Johnson

*Institut Laue-Langevin, BP 156, S. Cass Ave., 38042 Grenoble Cedex 9, France*

Received 28 September 2003; received in revised form 7 January 2004; accepted 14 January 2004

**Abstract**

The structure of the "Type III" $\delta$-$Bi_2O_3$-related superstructure phase in the system $Bi_2O_3$–$Nb_2O_5$ is presented. A starting model was constructed by considering the crystal-chemistry of the system in the context of symmetry constraints determined by electron diffraction. After applying initial distortions, this could be Rietveld-refined against a combination of synchrotron X-ray and time-of-flight neutron powder diffraction data. The undistorted starting model was independently optimized using solid-state ab initio energy calculations, giving a fully optimized structure in excellent agreement with that obtained by Rietveld refinement. This dual approach both validates the structure and demonstrates the value of combining accurate total energy calculations with traditional refinement techniques for the solution of complex structures using powder diffraction data. The structure ($Bi_{94}Nb_{32}O_{221}$, $Z = 1$, $I\bar{4}m2$ (#119), $a = 11.52156(18)$, $c = 38.5603(6)$ Å) consists of interacting corner-connected strings of $NbO_6$ octahedra along $\langle 110 \rangle_F$ directions of the FCC subcell, and can be described as a hybrid of fluorite and pyrochlore types.


*Keywords:* Bismuth niobium oxide; Delta-$Bi_2O_3$; Superstructure; Rietveld-refinement; Structure validation

## 1. Introduction

The high-temperature form of bismuth oxide, $\delta$-$Bi_2O_3$, is one of the best oxygen ion conductors known [1–3]. It has a face-centered cubic (FCC), fluorite-type structure, with 25% average oxygen vacancies accounting for its anionic conduction properties [4,5]. $\delta$-$Bi_2O_3$ cannot be quenched to room temperature, however, its fluorite-related structure and ionic conduction properties are approximately preserved at room temperature in some bismuth-rich phases in binary oxide systems involving certain transition metal oxides [2]. These phases have modulated structures based on an underlying fluorite-related substructure.

Many of these phases exist in solid solutions, and the volatility of $Bi_2O_3$ to sublimation makes stoichiometric control of syntheses rather difficult. Furthermore, the presence of complex modulated structures has led naturally to electron diffraction (ED) and high-resolution transmission electron microscopy (HRTEM) as the predominant analytical techniques [6–14]. As these techniques only examine one crystallite at a time, it is difficult to relate their results to those of bulk techniques such as X-ray powder diffraction (XRD) and neutron powder diffraction (NPD) necessary to determine the crystallographic phase diagrams.

As a prelude to studying some of these systems, we performed a careful synthetic and crystallographic study [15] in order to obtain single-phase powder samples from which we could be certain that local (ED) and bulk (XRD, NPD) crystallographic data would be consistent. The solution of a number of phases, and the availability of ED, synchrotron-XRD (S-XRD) and NPD data for many others, eventually permitted the formulation of a crystal-chemical scheme [16]. In this scheme, the substitution of transition metal cations such as $Nb^{5+}$ for $Bi^{3+}$ leads to a reduction of the 25% oxygen vacancies found in fluorite-type $\delta$-$Bi_2O_3$. At the same time, the octahedral coordination environment strongly preferred by $Nb^{5+}$ leads to distortions of the fluorite-type (cubic) oxygen lattice. Distortions can be minimized by organizing the $NbO_6$ octahedra into corner-connected chains along $\langle 110 \rangle_F$ directions of the fluorite-type unit cell, particularly when they interact to form tetrahedra of octahedra. This process is

*Corresponding author. Fax: +33-4-76-20-76-48.
*E-mail address:* ling@ill.fr (C.D. Ling).

0022-4596/$ - see front matter © 2004 Elsevier Inc. All rights reserved.
doi:10.1016/j.jssc.2004.01.003

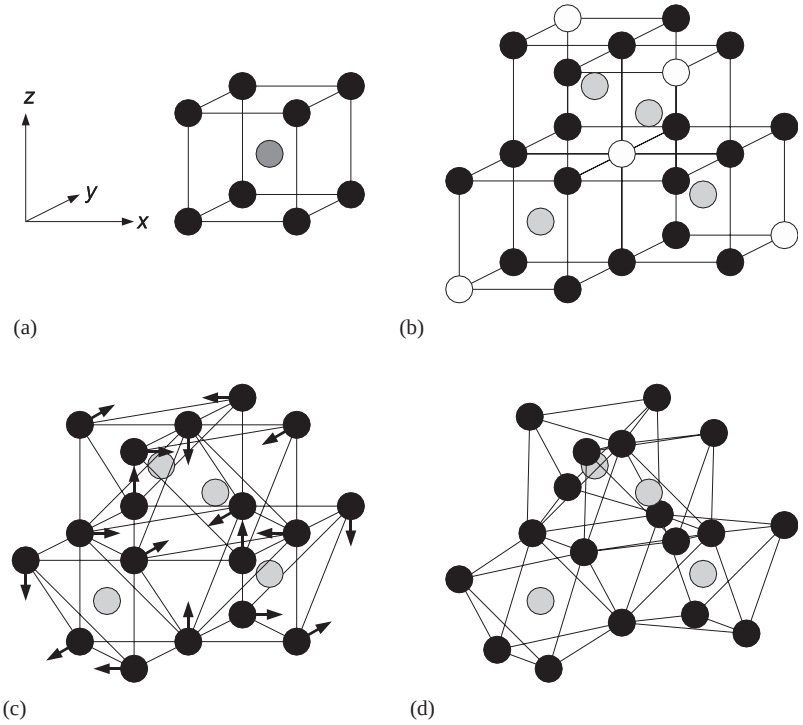


Fig. 1. Scheme for the incorporation of a pyrochlore-type structural motif into a fluorite-type average structure. (a) The cubic oxygen (black) coordination of bismuth (dark grey) in the fluorite-type average structure. (b) The arrangement of oxygen vacancies (white) within the fluorite-type oxygen lattice surrounding a tetrahedron of transition metal atoms (light grey), reducing the cubic coordination to octahedral coordination. (c) Co-operative oxygen atom displacive relaxations. (d) The resulting tetrahedron of octahedra.

illustrated in Fig. 1. The ultimate extension of this scheme is the conversion of fluorite-type into pyrochlore-type, although this is never actually achieved in these systems due to the adoption of other structure types above $\sim$25% doping [11].

Thus, although these structures are defined by compositional ordering in the metal atom array, the driving force behind the adoption of a given structure at a given stoichiometry is in fact vacancy ordering within the oxygen atom array (Fig. 1).

An appropriate test of a crystal-chemical scheme such as this is to use it to propose a model for an unsolved structure and then test the model against data. In this article, we present a model for the Type III phase in the $Bi_2O_3$–$Nb_2O_5$ system, of nominal composition $Bi_3NbO_7$, and refine it satisfactorily against a combination of S-XRD and NPD data.

Finally, in view of the complexity of the structure and the use of powder diffraction data, we sought complimentary evidence that the structure was chemically reasonable. We used a computational approach based on solid-state quantum chemistry calculations, which allow a parameter-free description of the inter-atomic interactions. The starting model was optimized by minimizing the total energy and the residual forces acting on the atoms. The optimized structure is in excellent agreement with the refined structure.

## 2. Experimental

A powder sample of $Bi_3NbO_7$ was prepared by solid-state reaction of a mixture of $Bi_2O_3$ (Koch-Lite 99.998%) and $Nb_2O_5$ (Aldrich 99.99%) at mole ratio 3:1 in a platinum crucible at 1103 K for 0.5 h. The sample was quenched to room temperature, reground, annealed in a sealed platinum vessel at 1173 K for 96 h, and again quenched to room temperature. A homogeneous yellow powder was obtained and identified as single-phase Type III $Bi_2O_3$–$Nb_2O_5$ by XRD [15].

S-XRD data were collected at Beam Line 20B at the Photon Factory in Tsukuba, Japan. The pattern was collected across three image plates at $\lambda = 1.4986$ Å. Si (NBS 640) was used as an internal standard. NPD data were collected on the time-of-flight instruments HRPD [17] and POLARIS [18] at ISIS (Rutherford Appleton Laboratories, UK). Refinements were carried out using the GSAS program [19] against data from the 30–130 ms TOF window with the backscattering detector of HRPD (for high resolution at short $d$-spacings) and the A (35°) detector bank of POLARIS (for long $d$-spacings).

Total energy calculations for the solid state were performed with VASP [20,21], which implements density functional theory (DFT) to find the ground state electronic density for a given configuration of atoms. The generalized gradient approximation of Perdew and

Wang (PW91) [22] for the exchange-correlation energy and Vanderbilt-type ultrasoft pseudopotentials [23] were used. For the plane wave basis set, the energy cutoff was determined by oxygen (270 eV) and only the gamma point was retained for calculations in reciprocal space. The ground state electronic density is obtained in a 'single point energy' (SPE) calculation, which also gives the forces acting on all atoms. Geometry optimization is then a sequence of SPE calculations. The conjugate gradient algorithm was used in the initial phase of minimization, followed by a quasi-Newton (RMM-DIIS) algorithm for a more precise geometry optimization. All calculations were performed on a dual processor ($2 \times 2$ Ghz Pentium IV) LINUX machine with 1.5 Gb of memory.

## 3. Modelling

Type III $Bi_2O_3$–$Nb_2O_5$ is clearly an ordered superstructure of fluorite-type $\delta$-$Bi_2O_3$ [7,15], therefore, the possibility exists of determining the structure absolutely given sufficient data. An attempt was made by Zhou et al. [7], who used image-matching/multi-slice methods with HRTEM and ED data to propose a model based on a pyrochlore-type cluster motif similar to the one presented here, but concentrating on tetrahedra of $NbO_6$ octahedra rather than $\langle 110 \rangle_F$ chains of $NbO_6$ octahedra. The interaction of these clusters creates some perovskite-type regions, such that this model appears to be a composite of fluorite, pyrochlore and perovskite types. This appeared reasonable given that the parent structure was clearly fluorite-type, that the slightly more bismuth-rich Type II phase was thought to contain such clusters [13,15] and that the slightly more bismuth-poor Type IV phase was thought to contain perovskite-type units [11]. We decided to re-examine the structure of this phase in light of a recent re-interpretation of the relationship of the Type II structure to pyrochlore-type [24].

Type II $Bi_2O_3$–$Nb_2O_5$ is now known to be a three-dimensionally incommensurate modulation of fluorite-type $\delta$-$Bi_2O_3$, based on corner-connected chains of $NbO_6$ octahedra along $\langle 110 \rangle_F$ directions of the FCC subcell [24]. It was shown [24] that there is a probable relationship between the primary modulation wave vector of the Type II $Bi_2O_3$–$Nb_2O_5$ phase and that of Type III. The first stage in arriving at a structural model for Type III was therefore to consider Type II.

The unit cell of Type III can be described as an $F$-centered $3 \times 3 \times 7$ supercell of fluorite-type, or alternatively as a $3/2(\mathbf{a}_F + \mathbf{b}_F)$, $3/2(-\mathbf{a}_F + \mathbf{b}_F)$, $7\mathbf{c}_F$ $I$-centered supercell. Either description is incompatible with a commensurate version of Type II, which would be cubic. Previous HRTEM work [7] indicates the way in which this incompatibility might be resolved; the structure appears to be 'layered', with a repeat of 3.5 fluorite-type unit cells. The observed image contrast implies the presence of a bismuth-rich layer in the metal atom array twice *per* unit cell perpendicular to the long ($c$) axis. The remaining metal atoms in the unit cell therefore comprise two $3 \times 3 \times 3$ fluorite-type blocks, symmetrically related by the $I$-centering of the $3 \times 3 \times 7$ Type III supercell.

Modelling of Type III began by treating this $3 \times 3 \times 3$ fluorite-type block analogously to Type II. In terms of the equations of Withers et al. [24], this corresponds to the choice $\varepsilon = 1/3$. The superspace group symmetry of Type II $P{:}Fm\bar{3}m{:}Fd\bar{3}m$ can then be reduced to a conventional space group symmetry for certain choices of $\delta_1$, $\delta_2$ and $\delta_3$. The highest possible resultant $3 \times 3 \times 3$ space group symmetry consistent with a tetragonal $3 \times 3 \times 7$ supercell is $F\bar{4}3m$, obtained when $\delta_1 = \delta_2 = -1/8$, $\delta_3 = 3/8$. The $\bar{4}3m$ point group symmetry of this space group is essentially that of a tetrahedron.

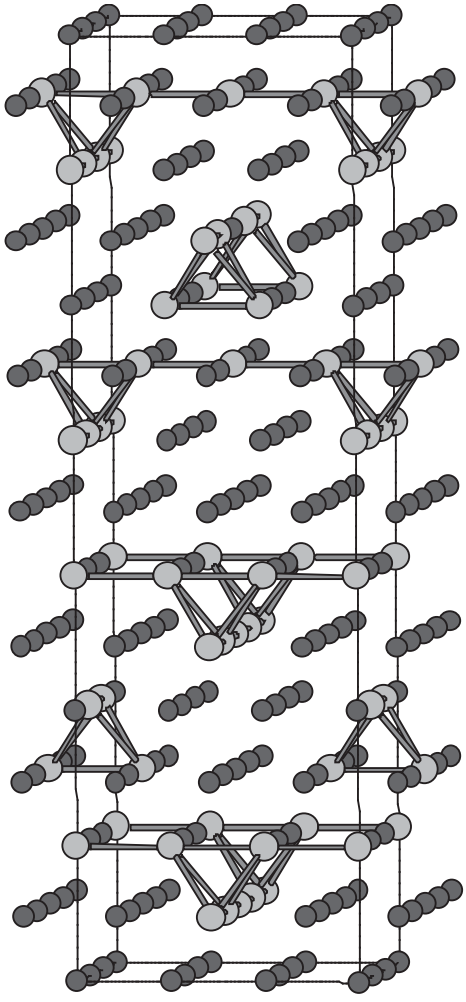

Fig. 2. The metal atom compositional ordering model of the Type III $Bi_2O_3$–$Nb_2O_5$ phase viewed close to the $[010] \equiv [110]_F$ direction. Nb–Nb nearest neighbor contacts are shown. Bismuth atoms are darker than niobium atoms.

Incorporating two such $F\bar{4}3m$ blocks into the $3 \times 3 \times 7$ supercell, and taking into consideration its overall $F$-centering, the resultant space group symmetry reduces to $F\bar{4}2m$ with respect to the $3 \times 3 \times 3$ supercell, or $I\bar{4}m2$ (#119) with respect to the $3/2(\mathbf{a}_F + \mathbf{b}_F)$, $3/2(-\mathbf{a}_F + \mathbf{b}_F)$, $7\mathbf{c}_F$, $I$-centered supercell. This symmetry lowering can be thought of in terms of 'stretching' a tetrahedron along its $\bar{4}$ axis; its $\bar{4}$ axis, 2-fold axis and mirror plane are preserved but its three-fold axis is broken. The space group $I\bar{4}m2$ is compatible with selected area ED observations (Fig. 5 of [15]), which suggested a maximum symmetry space group $I4/mmm$ (adding an inversion center to a point group symmetry of $\bar{4}m2$ implies Laue symmetry of $4/mmm$). The space group symmetry is lowered by breaking the mirror plane perpendicular to $c$, a symmetry element that was not compatible with the $3 \times 3 \times 3$ block concept. The presence or otherwise of an inversion center is difficult to detect by selected area ED.

This $I$-centered $(3/2(\mathbf{a}_F + \mathbf{b}_F),\ 3/2(-\mathbf{a}_F + \mathbf{b}_F), 7\mathbf{c}_F)$ cell contains $(3 \times 3 \times 7) \times 2 = 126$ metal atom sites, of which 32 (25.4%) should be Nb to most closely match the composition determined [15] from starting materials in synthesis as 25% and by energy dispersive X-ray analysis (EDXA) as 25.5(2)%. The proposed model calls for two of the 14 metal atom layers perpendicular to the long axis $c$, at $z = 0$ and $1/2$, to be pure Bi. The $3 \times 3 \times 3$ fluorite-type blocks should therefore each contain 32 Nb atoms, i.e. 29.6%.

Fourier difference techniques were used with low-angle (5–45°$2\theta$) synchrotron XRD data in order to find a metal atom compositional ordering pattern that satisfied both the low-angle XRD data and the required composition. One solution above all others investigated was found to give a remarkably good fit to the low-angle satellite reflections, ignoring any displacive modulation away from the fluorite-type subcell positions. This model is shown in Fig. 2 in the standard $I\bar{4}m2$ setting.

## 4. Refinement

The fact that X-ray scattering factors are proportional to atomic number means that only ~15% of the total X-ray scattering from Type III $Bi_2O_3$–$Nb_2O_5$ comes from the oxygen lattice. This has the disadvantage that the oxygen lattice (the most important part of the structure) can never be refined using S-XRD data; however, it has the advantage that the Bi–Nb compositional ordering is easily resolved. In contrast, the neutron scattering lengths of Bi, Nb and O are all comparable. This structure is therefore an ideal case in which to exploit the complementarity of neutrons and X-rays.

A stepwise approach was used. Firstly, atomic positions in the metal atom array, with the compositional ordering determined in the previous section (Fig. 2), were Rietveld-refined against S-XRD data.

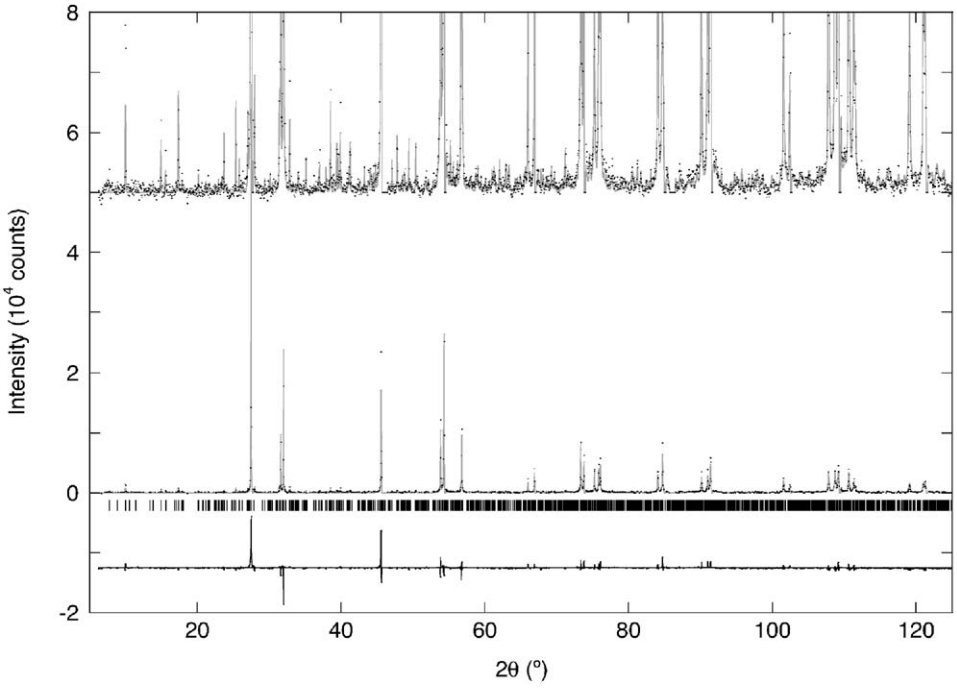


Fig. 3. Observed (black dots), calculated (grey line) and difference (bottom) synchrotron XRD ($\lambda = 1.4986$ Å) profiles for the Rietveld-refined metal-atom array of the Type III $Bi_2O_3$–$Nb_2O_5$ phase. The upper set of observed and calculated profiles, magnified by a factor of 20, demonstrate the amount of information contained in the modulation peaks. Peaks due to the Si standard have been excluded.

A global isotropic displacement parameter was also refined. The observed, calculated and difference S-XRD profiles for the Rietveld-refined metal atom arrays are shown in Fig. 3. Refinement statistics were $R_p = 0.0365$, $wR_p = 0.0588$, $R(F^2) = 0.1250$, and $\chi^2 = 6.19$. The quality of the fit confirmed the compositional ordering model.

Next, vacancies were introduced into the fluorite-type oxygen lattice around Nb sites according to the scheme shown in Fig. 1. This gave a model of composition $Bi_{94}Nb_{32}O_{222}$, which is slightly oxygen-rich (stoichiometry would require $Bi_{94}Nb_{32}O_{221}$). The required single oxygen vacancy in the unit cell is not compatible with the space group $I\bar{4}m2$), and was therefore treated as disordered. Unsurprisingly, attempts to Rietveld-refine this undistorted model against NPD data were unsuccessful. This is because, in the absence of any initial phasing, the least-squares refinement has no way of knowing in which direction to displace the oxygen atoms from their ideal fluorite-type positions. The very large number of possible initial displacements in this complex structure means that the chances of converging on the correct minimum are extremely small.

The crystal-chemical scheme shown in Fig. 1 was used to determine a set of (small) initial displacements for the 15 crystallographically independent oxygen atoms directly associated with Nb sites. This distorted model could be successfully Rietveld-refined against NPD data while the metal atom positions were fixed at the positions refined against S-XRD data. Isotropic atomic displacement parameters (ADPs) were constrained to be equal for each atomic type and refined.[1] Finally, all atomic positions were freely refined. The single disordered oxygen vacancy in the unit cell could not be localized to a specific oxygen site, and was therefore refined as being delocalized over all oxygen sites not directly coordinated to Nb.

The observed, calculated and difference NPD profiles for the final Rietveld-refined structure of Type III $Bi_2O_3$–$Nb_2O_5$ are shown in Fig. 4. Refinement statistics for 107 variables were $R_p = 0.0522$, $wR_p = 0.0686$, $R(F^2) = 0.0876$, and $\chi^2 = 10.73$. Fractional coordinates, $U_{iso}$ values and site multiplicities are presented in Table 1. Final refined unit cell parameters in space group #119 $I\bar{4}m2$ were $a = 11.52156(18)$ and $c = 38.5603(6)$ Å. The complete structure is shown in Fig. 5 with Bi atoms, O atoms, and solid $NbO_6$ octahedra. Fig. 6 shows part of the structure in the same projection with only the $NbO_6$ octahedra, while Fig. 7 shows the structure projected along the $[110] \equiv [100]_F$ direction in order to illustrate the distorted, oxygen deficient, fluorite-type lattice. Bond distances are summarized in Table 2. Further details can be found in the deposited crystallographic information file (CIF).

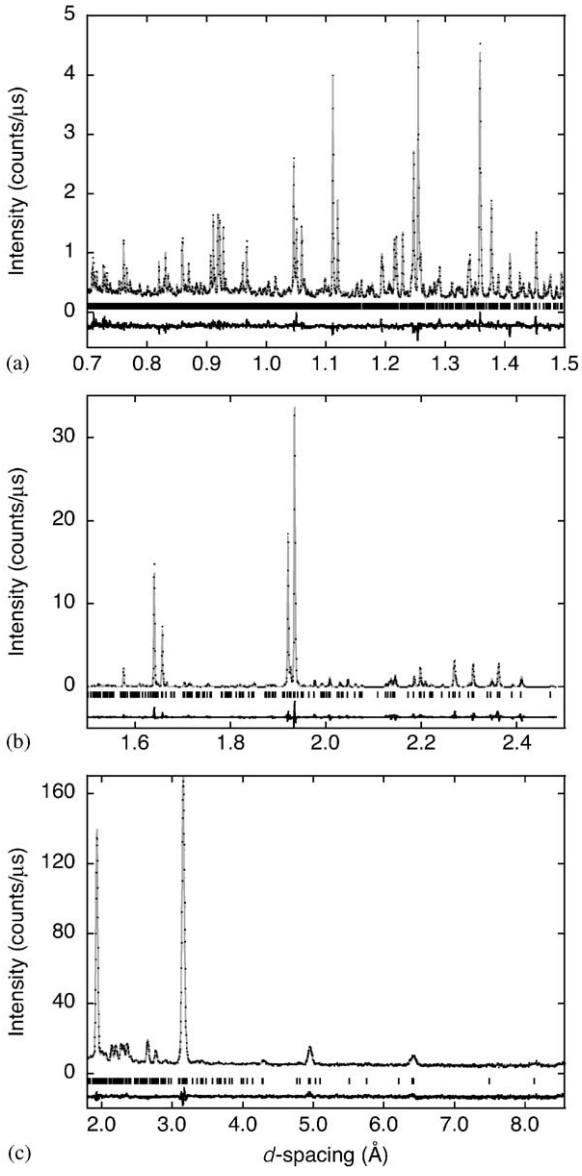


Fig. 4. Observed (black dots), calculated (grey line) and difference (bottom) neutron powder diffraction profiles for the final Rietveld-refined structure of the Type III $Bi_2O_3$–$Nb_2O_5$ phase using (a,b) the 30–130 ms TOF window with the backscattering detector of HRPD and (c) the 35° detector bank of POLARIS.

## 5. Calculations

Structural optimizations with VASP were performed in the primitive setting of the experimentally determined

[1] Refinement of all ADPs independently led to a distribution $0.01 \leqslant U_{iso} \leqslant 0.09$, however, standard deviations on these refined values largely overlapped. The constrained refinement has therefore been chosen for publication. Given that the reduction in the $\chi^2$ value was not large (from 10.8 to 8.7), no ADPs became negative or excessively large, and no significant atomic shifts occurred, we are confident that these constraints do not conceal any fundamental problems with the refinement.

Table 1
Fractional coordinates, $U_{iso}$ values and site multiplicities for the final Rietveld-refined structure of the Type III $Bi_2O_3$–$Nb_2O_5$ phase

| Atom | $x$ | $y$ | $z$ | $100U_{iso}$ | Mult. |
|---|---|---|---|---|---|
| Nb(1) | 0.6624(9) | 0 | 0.14462(21) | 0.66(5) | 8 |
| Nb(2) | 1/2 | 0.1654(7) | 0.07151(24) | 0.66(5) | 8 |
| Nb(3) | 0 | 0 | 0.1419(4) | 0.66(5) | 4 |
| Nb(4) | 0.6671(8) | 0 | 0.7157(2) | 0.66(5) | 8 |
| Nb(5) | 1/2 | 1/2 | 0.0799(3) | 0.66(5) | 4 |
| Bi(1) | 0.8373(6) | 0.1739(6) | 0.21559(15) | 1.99(3) | 16 |
| Bi(2) | 0.6660(9) | 0 | 0.2865(2) | 1.99(3) | 8 |
| Bi(3) | 0.1684(6) | 0.1684(6) | 1/2 | 1.99(3) | 8 |
| Bi(4) | 0.6670(8) | 0 | 0.85939(18) | 1.99(3) | 8 |
| Bi(5) | 0.6627(7) | 0 | 0.5725(2) | 1.99(3) | 8 |
| Bi(6) | 0 | 0 | 0.2778(3) | 1.99(3) | 4 |
| Bi(7) | 0.3339(10) | 0 | 0.99931(17) | 1.99(3) | 8 |
| Bi(8) | 0 | 0 | 0 | 1.99(3) | 2 |
| Bi(9) | 0.1616(4) | 0.1669(5) | 0.07143(18) | 1.99(3) | 16 |
| Bi(10) | 0.1742(5) | 0.1602(6) | 0.35760(14) | 1.99(3) | 16 |
| O(1) | 1/2 | 0 | 0.1666(4) | 2.69(3) | 4 |
| O(2) | 0 | 0.1294(10) | 0.1038(3) | 2.69(3) | 8 |
| O(3) | 0 | 0.1259(9) | 0.1689(2) | 2.69(3) | 8 |
| O(4) | 0.3113(7) | 0.1259(6) | 0.1801(2) | 2.69(3) | 16 |
| O(5) | 0 | 1/2 | 0.1955(4) | 2.69(3) | 4 |
| O(6) | 0.1236(8) | 0.3764(8) | 1/4 | 2.69(3) | 8 |
| O(7)* | 0 | 0.2010(10) | 0.0426(3) | 2.69(3) | 8 |
| O(8) | 1/2 | 0.3297(10) | 0.0953(3) | 2.69(3) | 8 |
| O(9) | 0.2089(6) | 0.3724(6) | 0.1812(2) | 2.69(3) | 16 |
| O(10)* | 1/2 | 0.3175(10) | 0.1738(3) | 2.69(3) | 8 |
| O(11)* | 0.1814(6) | 0.3259(6) | 0.03081(19) | 2.69(3) | 16 |
| O(12)* | 0.3150(7) | 0.1850(7) | 1/4 | 2.69(3) | 8 |
| O(13)* | 0.1596(9) | 0 | 0.0323(3) | 2.69(3) | 8 |
| O(14)* | 0 | 1/2 | 0.1141(4) | 2.69(3) | 4 |
| O(15)* | 1/2 | 0.3331(9) | 0.2607(3) | 2.69(3) | 8 |
| O(16) | 0.3798(7) | 0.1207(7) | 0.1099(2) | 2.69(3) | 16 |
| O(17)* | 0 | 1/2 | 0.0422(4) | 2.69(3) | 4 |
| O(18) | 0.3742(7) | 0.2024(7) | 0.04250(18) | 2.69(3) | 16 |
| O(19) | 0.1720(9) | 0 | 0.1300(2) | 2.69(3) | 8 |
| O(20) | 0.3668(9) | 1/2 | 0.1238(2) | 2.69(3) | 8 |
| O(21)* | 0.1521(7) | 0.3198(8) | 0.1063(2) | 2.69(3) | 16 |
| O(22) | 0.3748(9) | 1/2 | 0.0504(2) | 2.69(3) | 8 |
| O(23) | 1/2 | 0 | 0.0609(4) | 2.69(3) | 4 |
| O(24) | 0.3221(10) | 1/2 | 0.2355(3) | 2.69(3) | 8 |
| O(25)* | 1/2 | 0 | 1/4 | 2.69(3) | 2 |

Space group #119 $I\bar{4}m2$, $a = 11.52156(18)$, $c = 38.5603(6)$ Å. $U_{iso}$ values were constrained to be equal for each element. Note that the space group implies composition $Bi_{94}Nb_{32}O_{222}$ but stoichiometry requires $Bi_{94}Nb_{32}O_{221}$; the single disordered oxygen vacancy in the unit cell that this implies could not be localized a specific oxygen site, and was therefore refined as being delocalized over all oxygen sites not directly coordinated to Nb (marked *, with occupancies 98.8%).

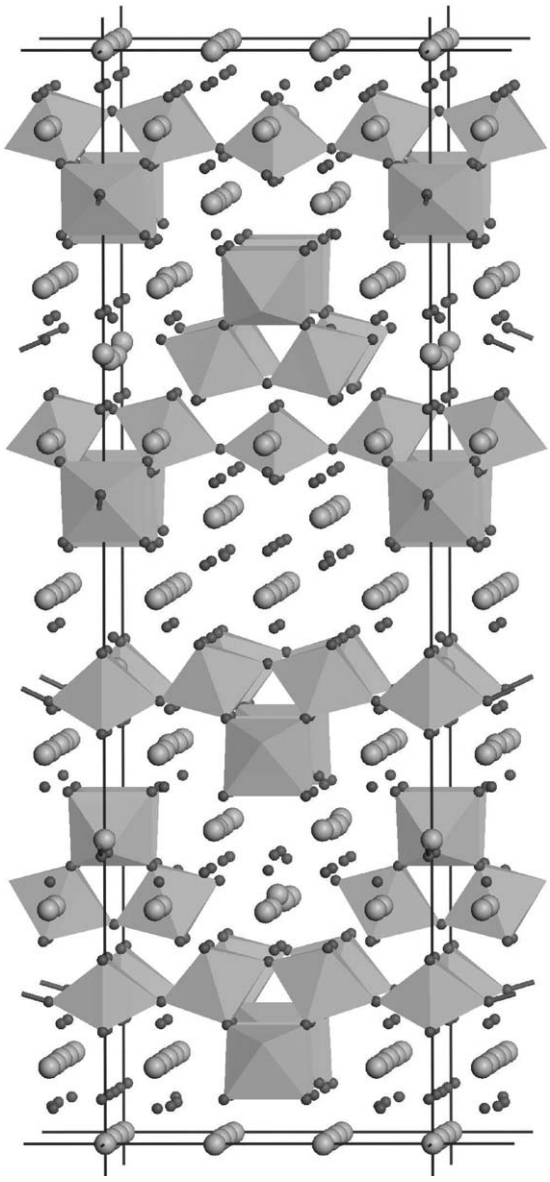

Fig. 5. The final Rietveld-refined structure of the Type III $Bi_2O_3$–$Nb_2O_5$ phase viewed close to the $[010] \equiv [110]_F$ direction (space group #119 $I\bar{4}m2$, $a = 11.52156(18)$, $c = 38.5603(6)$ Å). Oxygen atoms are black, $NbO_6$ octahedra are light grey and bismuth atoms are dark grey. Note that the space group implies composition $Bi_{94}Nb_{32}O_{222}$ but stoichiometry requires $Bi_{94}Nb_{32}O_{221}$; the single disordered oxygen vacancy in the unit cell that this implies could not be localized to a specific oxygen site, and was therefore refined as being delocalized over all oxygen sites not directly coordinated to Nb.

unit cell ($a = b = c = 20.9256$ Å, $\alpha = \beta = 148.05°$, $\gamma = 45.81°$, 174 independent atoms). The initial coordinates were taken from the undistorted starting model (with oxygen vacancies introduced but leaving the remaining oxygen atoms at their ideal fluorite-type positions). Recall that Rietveld-refinements of this undistorted structure never converged; success was only achieved after initial displacements were painstakingly applied by hand. Within about 50 cycles of geometry optimization (about one week on the dual processor PC) a stable structure was obtained with residual forces smaller than $F_{max} = 0.04$ eV/Å (mean residual force $F_{ave} = 0.006$ eV/Å). The final calculated structure was extremely close to the final Rietveld-refined structure. Offsets between equivalent atoms in the two structures are included in Table 3. The average offset for metal atoms is 0.065 Å and for oxygen atoms 0.085 Å.

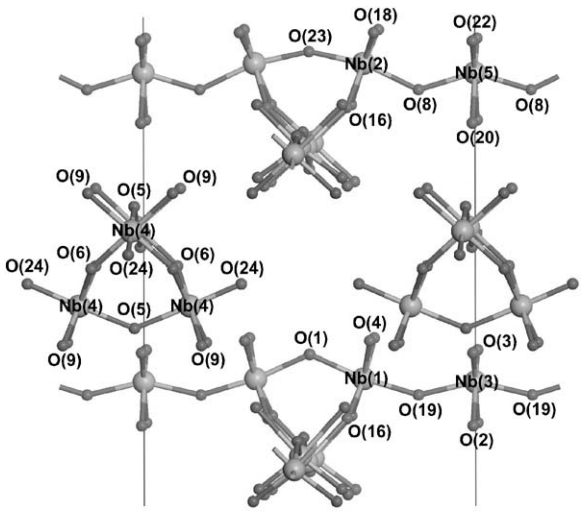


Fig. 6. Part of Fig. 5 ($-0.33 \leqslant x \leqslant 1.33$, $0.15 \leqslant y \leqslant 1.25$, $0.03 \leqslant z \leqslant 0.47$) showing the Nb–O connectivity (corresponding distances listed in Table 2). Bi atoms and O atoms not coordinated to Nb are excluded for clarity.

Although the final calculated structure was both stable and in good agreement with the final refined structure, from similar calculations on simpler structures, smaller residual forces were expected. Subsequent geometry optimization gave only minor atomic shifts and no significant improvement in the stability of the structure. The presence of significant residual forces in an otherwise stable and robust structure suggests that it is somewhat frustrated, stabilized by delicately balanced forces.

Empirical bond valence sums [25] for the Rietveld-refined and VASP-optimized structures of Type III $Bi_2O_3$–$Nb_2O_5$ are presented in Table 3, along with their deviations from expected values. For both the Rietveld-refined and VASP-optimized versions of the structure, the results show it to be reasonable, considering its complexity and the fact that it represents a compromise between the fluorite and pyrochlore structure-types. The mean absolute deviations from expected valences are 8.7% (Rietveld) and 8.4% (VASP), demonstrating again that the structure is reasonable and stable, but nonetheless slightly internally frustrated.

With respect to the single disordered oxygen vacancy in the unit cell, note that the calculated bond valences do not support the presence of either $Bi^{5+}$ or $Nb^{5+}$ on any of the Bi sites (which would allow for an apparent oxygen overstoichiometry). Furthermore, attempts to localize the oxygen vacancy to sites coordinated to the most overbonded Bi sites were not successful in improving the Rietveld-refinements against NPD data. Note that this vacancy could not be introduced into the VASP model without creating a further supercell, which would have made the calculations impractically slow.

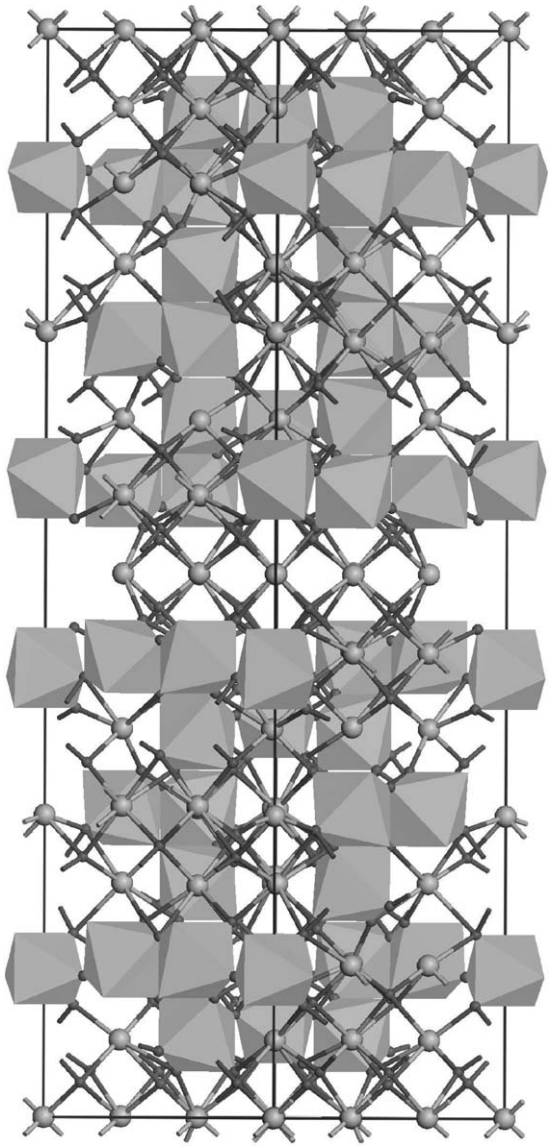

Fig. 7. The final Rietveld-refined structure viewed along the $[110] \equiv [100]_F$ direction, showing the distorted, oxygen deficient, fluorite-type lattice. Bi atoms have approximately cubic coordination, with either 0, 1 or 2 corners missing (see Table 2). Oxygen atoms are black, $NbO_6$ octahedra are light grey and bismuth atoms are dark grey.

## 6. Discussion

The Type III phase is the most Nb-rich phase in the $Bi_2O_3$–$Nb_2O_5$ system to preserve the fluorite-related substructure of $\delta$-$Bi_2O_3$ (Fig. 7). The solution of this structure fixes its composition as a line phase on the $Bi_2O_3$–$Nb_2O_5$ phase diagram as $Bi_{94}Nb_{32}O_{221}$, or 25.4% $Nb_2O_5$, consistent with the EDXA analysis (25.4(2)%) [15] and with the result of Castro et al. [26], who studied a single crystal that was clearly of crystallographic Type II and chemically determined to be 25% $Nb_2O_5$.

On consideration, it is remarkable that this Type III phase is stable. Sitting at the end of the broad Type II

Table 2
Bond lengths for the final Rietveld-refined structure

| Bond | Length (Å) | Mult. | Bond | Length (Å) | Mult. |
|---|---|---|---|---|---|
| Nb(1)–O(1) | 2.061(11) | 1 | Bi(4)–O(3) | 2.624(14) | 1 |
| Nb(1)–O(4) | 2.015(9) | 2 | Bi(4)–O(5) | 2.862(15) | 1 |
| Nb(1)–O(16) | 1.992(10) | 2 | Bi(4)–O(9) | 2.906(8) | 2 |
| Nb(1)–O(19) | 1.984(14) | 1 | Bi(4)–O(14) | 2.179(12) | 1 |
| Nb(2)–O(8) | 2.109(15) | 1 | Bi(4)–O(21) | 2.200(9) | 2 |
| Nb(2)–O(16) | 2.091(11) | 2 | Bi(5)–O(11) | 2.580(10) | 2 |
| Nb(2)–O(18) | 1.885(10) | 2 | Bi(5)–O(14) | 2.467(14) | 1 |
| Nb(2)–O(23) | 1.944(9) | 1 | Bi(5)–O(17) | 2.209(12) | 1 |
| Nb(3)–O(2) | 2.092(14) | 2 | Bi(5)–O(21) | 2.455(10) | 2 |
| Nb(3)–O(3) | 1.801(14) | 2 | Bi(5)–O(22) | 2.588(13) | 1 |
| Nb(3)–O(19) | 2.032(11) | 2 | Bi(6)–O(10) | 2.811(13) | 2 |
| Nb(4)–O(5) | 2.078(12) | 1 | Bi(6)–O(15) | 2.429(13) | 2 |
| Nb(4)–O(6) | 2.007(7) | 2 | Bi(6)–O(24) | 2.112(12) | 2 |
| Nb(4)–O(9) | 2.042(9) | 2 | Bi(7)–O(7) | 2.226(15) | 1 |
| Nb(4)–O(24) | 1.945(14) | 1 | Bi(7)–O(11) | 2.392(8) | 2 |
| Nb(5)–O(8) | 2.045(12) | 2 | Bi(7)–O(13) | 2.377(15) | 1 |
| Nb(5)–O(20) | 2.290(13) | 2 | Bi(7)–O(17) | 2.494(14) | 1 |
| Nb(5)–O(22) | 1.840(13) | 2 | Bi(7)–O(18) | 2.903(9) | 2 |
| Bi(1)–O(3) | 2.656(9) | 1 | Bi(8)–O(7) | 2.839(12) | 4 |
| Bi(1)–O(4) | 2.261(10) | 1 | Bi(8)–O(13) | 2.220(10) | 4 |
| Bi(1)–O(6) | 2.721(11) | 1 | Bi(9)–O(2) | 2.282(8) | 1 |
| Bi(1)–O(9) | 2.697(10) | 1 | Bi(9)–O(7) | 2.204(8) | 1 |
| Bi(1)–O(12) | 2.204(9) | 1 | Bi(9)–O(11) | 2.421(9) | 1 |
| Bi(1)–O(15) | 2.203(8) | 1 | Bi(9)–O(13) | 2.445(9) | 1 |
| Bi(1)–O(24) | 2.660(10) | 1 | Bi(9)–O(16) | 2.966(10) | 1 |
| Bi(2)–O(1) | 2.632(15) | 1 | Bi(9)–O(18) | 2.722(10) | 1 |
| Bi(2)–O(4) | 2.568(9) | 2 | Bi(9)–O(19) | 2.969(10) | 1 |
| Bi(2)–O(10) | 2.320(15) | 1 | Bi(9)–O(21) | 2.220(11) | 1 |
| Bi(2)–O(12) | 2.564(8) | 2 | Bi(10)–O(4) | 2.743(10) | 1 |
| Bi(2)–O(15) | 2.650(14) | 1 | Bi(10)–O(8) | 2.591(9) | 1 |
| Bi(2)–O(25) | 2.376(10) | 1 | Bi(10)–O(9) | 2.191(10) | 1 |
| Bi(3)–O(11) | 2.101(10) | 2 | Bi(10)–O(10) | 2.210(8) | 1 |
| Bi(3)–O(18) | 2.268(8) | 2 | Bi(10)–O(16) | 2.714(10) | 1 |
| Bi(3)–O(22) | 2.790(9) | 2 | Bi(10)–O(20) | 2.154(8) | 1 |
| Bi(4)–O(2) | 2.742(13) | 1 | Bi(10)–O(21) | 2.573(11) | 1 |

Table 3
Bond valence sums [25] for the final Rietveld-refined and VASP-optimized structures of the Type III $Bi_2O_3$–$Nb_2O_5$ phase, deviations from expected values (three for Bi, five for Nb and two for O), and offsets between equivalent atoms in the two structures

| Atom | Refinement | | VASP-optimized | | Offset (Å) |
|---|---|---|---|---|---|
| | Calculated | Deviation (%) | Calculated | Deviation (%) | |
| Nb(1) | 4.604 | 8 | 4.582 | 8 | 0.035 |
| Nb(2) | 4.877 | 2 | 4.683 | 6 | 0.059 |
| Nb(3) | 5.360 | 7 | 4.586 | 8 | 0.015 |
| Nb(4) | 4.495 | 10 | 4.657 | 7 | 0.082 |
| Nb(5) | 4.534 | 9 | 4.461 | 11 | 0.111 |
| Bi(1) | 2.932 | 2 | 2.984 | 1 | 0.047 |
| Bi(2) | 2.579 | 14 | 2.612 | 13 | 0.054 |
| Bi(3) | 3.522 | 17 | 3.083 | 3 | 0.081 |
| Bi(4) | 3.054 | 2 | 2.481 | 17 | 0.035 |
| Bi(5) | 2.642 | 12 | 2.691 | 10 | 0.064 |
| Bi(6) | 3.022 | 1 | 3.018 | 1 | 0.213 |
| Bi(7) | 2.604 | 13 | 2.667 | 11 | 0.032 |
| Bi(8) | 3.428 | 14 | 3.104 | 3 | 0 |
| Bi(9) | 3.240 | 8 | 2.785 | 7 | 0.062 |
| Bi(10) | 3.276 | 9 | 2.966 | 1 | 0.089 |
| O(1) | 1.804 | 10 | 1.718 | 14 | 0.039 |
| O(2) | 2.003 | 0 | 1.849 | 8 | 0.115 |
| O(3) | 2.035 | 2 | 1.712 | 14 | 0.321 |
| O(4) | 1.840 | 8 | 1.858 | 7 | 0.081 |
| O(5) | 1.530 | 23 | 1.446 | 28 | 0.034 |
| O(6) | 1.910 | 5 | 1.794 | 10 | 0.033 |
| O(7) | 2.317 | 16 | 1.887 | 6 | 0.208 |
| O(8) | 1.796 | 10 | 1.841 | 8 | 0.018 |
| O(9) | 1.796 | 10 | 1.729 | 14 | 0.055 |
| O(10) | 2.146 | 7 | 1.843 | 8 | 0.257 |
| O(11) | 2.108 | 5 | 2.016 | 1 | 0.075 |
| O(12) | 2.056 | 3 | 2.094 | 5 | 0.126 |
| O(13) | 1.950 | 3 | 2.311 | 16 | 0.100 |
| O(14) | 2.310 | 16 | 2.182 | 9 | 0.003 |
| O(15) | 2.101 | 5 | 1.972 | 1 | 0.151 |
| O(16) | 1.70 | 15 | 1.682 | 16 | 0.036 |
| O(17) | 2.154 | 8 | 1.972 | 1 | 0.010 |
| O(18) | 1.997 | 0 | 1.757 | 12 | 0.042 |
| O(19) | 1.732 | 13 | 1.641 | 18 | 0.060 |
| O(20) | 2.073 | 4 | 1.831 | 8 | 0.047 |
| O(21) | 2.112 | 6 | 2.065 | 3 | 0.113 |
| O(22) | 1.777 | 11 | 1.675 | 16 | 0.031 |
| O(23) | 1.830 | 8 | 1.734 | 13 | 0.095 |
| O(24) | 2.30 | 15 | 2.003 | 0 | 0.087 |
| O(25) | 1.888 | 6 | 2.126 | 6 | 0 |

solid-solution range (6–25% $Nb_2O_5$), it uses the same motif of $\langle 110 \rangle_F$ strings of $NbO_6$ octahedra to preserve the fluorite-type substructure, but in a far less elegant manner. It requires a significant lowering of symmetry, as a result of which the $\langle 110 \rangle_F$ strings are compromised and strained. Most obviously, the 'layered' nature of the structure precludes continuous octahedral strings with a component along the stacking ($c$) axis, reducing the number of independent $\langle 110 \rangle_F$ directions in which continuous $NbO_6$ octahedral strings are observed from three to two. Furthermore, the relative orientations of these directions is different; in Type II, each of the three $\langle 110 \rangle_F$ strings is perpendicular to a different $\langle 100 \rangle_F$ direction, whereas in Type III, both strings are perpendicular to the same $\langle 100 \rangle_F$ direction.[2] The two remaining string directions are also strained as a result of the 3-Nb repeat along $\langle 100 \rangle \equiv \langle 110 \rangle_F$. This odd-numbered repeat prevents the relaxed up–down–up–down arrangement of oxygen atoms connecting the corners of $NbO_6$ octahedrons in strings. Fig. 6 clearly shows the distorted $Nb(5)O_6$ and $Nb(3)O_6$ octahedra that bridge between more relaxed tetrahedra of $Nb(1)O_6$ and $Nb(2)O_6$ octahedra in a strained up–down–down–up–down–down arrangement. In fact, this strained bridging $NbO_6$ octahedra is only present in half the strings, as can be seen in Fig. 6.

[2] Note that pyrochlore-type itself can be constructed from either three interpenetrating $\langle 110 \rangle_F$ strings at 60° to one another, such as are found in Type II, or from two independent $\langle 110 \rangle_F$ strings at 90° to one another, such as are found in Type III; the two structures could therefore be considered as alternative expansions of pyrochlore-type for incorporation into fluorite-type.

Finally, there is the necessity to introduce a single disordered oxygen vacancy into the unit cell to comply with the metal stoichiometry. A preferred site for this oxygen vacancy could not be found, beyond the observation that it cannot be located on any oxygen site coordinated to a Nb site. It is therefore assumed to be evenly distributed over the remaining 10 independent oxygen sites with a total multiplicity of 82, i.e., these sites have 98.8% occupancy. This limited disorder is unavoidable without lowering the symmetry from $I\bar{4}m2$, something we cannot presently test. Symmetry lowering is clearly not justified by the available NPD data (which is among the highest-resolution available), and VASP calculations in a lower symmetry are not feasible in a reasonable time with available hardware. It can only be commented that this small imperfection epitomizes the delicately balanced nature of this structure.

## 7. Conclusion

The model proposed [16] for the structure of the Type III $Bi_2O_3$–$Nb_2O_5$ phase has been confirmed by Rietveld-refinement of S-XRD and NPD data. The same structure has been obtained from the starting model using ab initio energy calculations, validating both the structure and a the use of a complementary Rietveld-DFT approach for difficult structure determinations from powder diffraction data.

The unit cell (space group #119 $I\bar{4}m2$, $a = 11.52158(17)$, $c = 38.5603(6)$ Å) has composition $Bi_{94}Nb_{32}O_{221}$ (incorporating one disordered oxygen vacancy to comply with stoichiometry), clarifying the composition of the line phase on the $Bi_2O_3$–$Nb_2O_5$ phase diagram [15]. The structure consists of interacting corner-connected strings of $NbO_6$ octahedra along $\langle 110 \rangle_F$ directions of the FCC subcell. It can be described as a hybrid of the fluorite and pyrochlore structure types, in accordance with the crystal-chemical scheme on the basis of which it was proposed [16].

## References

[1] T. Takahashi, H. Iwakawa, T. Esaka, J. Electrochem. Soc. 124 (1977) 1563.
[2] T. Takahashi, H. Iwakawa, Mater. Res. Bull. 13 (1978) 1447.
[3] A.W. Sleight, Science 208 (4446) (1980) 895.
[4] G. Gattow, H. Schröder, Z. Anorg. Allg. Chem. 318 (1962) 176.
[5] H.A. Harwig, Z. Anorg. Allg. Chem. 444 (1978) 151.
[6] W. Zhou, D.A. Jefferson, J.M. Thomas, Proc. Roy. Soc. London Ser. A 406 (1986) 173.
[7] W. Zhou, D.A. Jefferson, J.M. Thomas, J. Solid State Chem. 70 (1987) 129.
[8] D. Tang, W. Zhou, J. Solid State Chem. 119 (1995) 311.
[9] W. Zhou, D.A. Jefferson, M. Alario-Franco, J.M. Thomas, J. Phys. Chem. 91 (1987) 512.
[10] W. Zhou, D.A. Jefferson, J.M. Thomas, Geophys. Monogr. 43 (1989) 113.
[11] W. Zhou, J. Solid State Chem. 101 (1992) 1.
[12] J. Gopalakrishnan, A. Ramanan, C.N.R. Rao, D.A. Jefferson, D.J. Smith, J. Solid State Chem. 55 (1984) 101.
[13] W. Zhou, J. Solid State Chem. 108 (1994) 381.
[14] D.J. Buttrey, D.A. Jefferson, J.M. Thomas, Mater. Res. Bull. 21 (1986) 739.
[15] C.D. Ling, R.L. Withers, S. Schmid, J.G. Thompson, J. Solid State Chem. 137 (1998) 42.
[16] C.D. Ling, J. Solid State Chem. 148 (1999) 380.
[17] R.M. Ibberson, W.I.F. David, K.S. Knight, The high resolution powder diffractometer (HRPD) at ISIS—a user's guide. Report RAL-92-031, Rutherford Appleton Laboratories, Chilton, Didcot, UK, 1992.
[18] S. Hull, R.I. Smith, W.I.F. David, A.C. Hannon, J. Mayers, R. Cywinski, Physics B 180–181 (1992) 1000.
[19] A.C. Larson, R.B. von Dreele, Software GSAS. The general structure analysis system, Los Alamos National Laboratory, Los Alamos, NM, 1991.
[20] G. Kresse, J. Furthmüller, Software VASP, Vienna, 1999, Phys. Rev. B 54 (1996) 11169;
G. Kresse, J. Furthmüller, Software VASP, Vienna, 1999, Comput. Mater. Sci. 6 (1996) 15.
[21] G. Kresse, J. Hafner, Phys. Rev. B 47 (1993) 558;
G. Kresse, J. Hafner, Phys. Rev. B 49 (1994) 14251.
[22] J.P. Perdew, Y. Wang, Phys. Rev. B 45 (1992) 13244.
[23] D. Vanderbilt, Phys. Rev. B 41 (1990) 7892.
[24] R.L. Withers, C.D. Ling, S. Schmid, Z. Kristallogr. 214 (5) (1999) 296.
[25] N.E. Brese, M. O'Keefe, Acta Crystallogr. B 47 (1991) 192.
[26] A. Castro, E. Aguardo, J.M. Rojo, P. Herrero, R. Enjalbert, J. Galy, Mater. Res. Bull. 33 (1998) 31.